Free Flight Testing and Performance Evaluation of a Passively Morphing Ornithopter

Aimy Wissa[1], Jared Grauer[2], Nelson Guerreiro[3], James Hubbard Jr.[3], Cornelia Altenbuchner[3], Yashwanth Tummala[4], Mary Frecker[4] and Richard Roberts[5]

[1]University of Illinois Urbana Champaign
1206 West Green Street, Urbana, Illinois 61801, awissa@illinois.edu
[2]NASA Langley Research Center, MS 308
Dynamic Systems and Controls Branch, Hampton, VA 23681
jared.a.grauer@nasa.gov
[3]University of Maryland,
100 Exploration Way, Hampton, VA, 23666, nelsong@umd.edu, jhubbard@nianet.org,
cornelia.altenbuchner@nasa.gov
[4]Pennsylvania State University, 314D Leonhard Building
University Park, PA, 18602, yash@psu.edu, mxf36@psu.edu
[5]Wright Patterson Air Force Base, Dayton, OH, 45433

ABSTRACT

Unmanned Aerial Vehicles (UAVs) are proliferating in both the civil and military markets. Flapping wing UAVs, or ornithopters, have the potential to combine the agility and maneuverability of rotary wing aircraft with excellent performance in the low Reynolds number flight regimes. The purpose of this paper is to present new free flight experimental results for an ornithopter equipped with single degree of freedom compliant spines. The compliant spines are designed and optimized in terms of mass, maximum von-Mises stress, and desired wing bending deflections. The spines are inserted in an experimental ornithopter wing leading edge spar, in order to achieve a set of desired kinematics during the up and down strokes of a flapping cycle. The ornithopter is flown at Wright Patterson Air Force Base in the Air Force Research Laboratory Small Unmanned Air Systems (SUAS) indoor flight facility. Vicon® motion tracking cameras are used to track the motion of the vehicle for four different wing configurations. The effect of the presence of the compliant spine on the wings and body kinematics, as well as the leading edge spar deflection during free flight is presented in this paper. Several metrics were used to evaluate the vehicle performance with various compliant spine designs inserted in the leading edge spar of the wings. Results show that passively morphing the wings, via adding compliance in the leading edge spar, does not require additional power expenditure and is beneficial to the overall vertical and horizontal propulsive force production.

1. INTRODUCTION

In recent years, flapping wing Small Unmanned Aerial Vehicles (SUAVs), or ornithopters, have shown the potential for advancing and revolutionizing SUAV performance in both the civil and military sectors [1]. Compared to fixed wing and rotary wing vehicles, an ornithopter is unique in that it can combine the agility and maneuverability of rotary wing aircraft with excellent performance in low Reynolds number flight regimes. These traits could yield optimized performance over multiple mission scenarios. Nature achieves such performance in birds using wing gaits or kinematics that are optimized for a particular flight condition [2, 3].

Modern designs for wing morphing in flapping wing SUAVs utilize rigid-link mechanisms, such as rigid four-bar mechanisms, or involve active morphing techniques [4-6]. Most active wing morphing

mechanisms for ornithopters have resulted in designs that are heavy and too complicated to be implemented during free flight and were limited to bench top tests [7, 8]. In contrast to rigid-link mechanisms and active approaches, the focus of the current research is on the implementation of a novel *passive* morphing technique using compliant mechanisms. Passive morphing is defined such that the shape change is a result of the operational loads the vehicle experiences during flight and not due to a separate actuation mechanism. When compared to active morphing, passive morphing mechanisms require no actuation energy expenditure, minimal weight addition and a significant reduction in complexity.

The overall goal of the research presented here is to increase the range and endurance of flapping wing SUAVs by employing passive bio-inspired structural modifications. The structural modification implemented in the ornithopter wings is in the form of a contact aided compliant mechanism that is designed to be inserted in the wings leading edge spar to mimic the function of an avian wrist. In this paper, free flight data comparing performance metrics for a test ornithopter with and without the compliant mechanism is presented. The data collected is used to assess the effect of the compliant mechanism on wing and body kinematics, and the vehicle's overall performance, as well as increase the understanding of the flight physics and dynamics of flapping wing unmanned vehicles. Wing kinematics data was previously collected on a bench top where the ornithopter fuselage was clamped to a six degree of freedom (DOF) load cell [9,10]. This paper is organized as follows: the research approach and a summary of the compliant spine design optimization are presented in Section 2. Section 3 then discusses the experimental procedures and ornithopter set-up. Lastly, Section 4 presents the free flight tests results of the baseline ornithopter kinematics and the effect of the compliant spine presence on the leading edge spar deflection and vehicle's overall performance.

2. RESEARCH APPROACH
2.1. Bio-inspired Approach to Passive Wing Morphing
The benefits and efficacy of passive wing morphing attained by introducing an asymmetry into the leading edge wing spar of a test ornithopter during the up and down strokes have been previously investigated in References 11 and 12. In Reference 11, Mueller et al. designed three different compliant hinges, each of these hinges allowed for bending during the upstroke only. Only one of these designs was successful enough to support flight, however the lift gains produced by this design also incurred some thrust penalties. Billingsely et al. installed passive torsional springs into the leading edge spar at the wing half span in order to exploit the advantages of wing surface area reduction during the upstroke [12]. These springs were designed to deflect during the upstroke only and lock during the downstroke. Wing bending during the upstroke reduces the wing relative area (i.e., the wing area perpendicular to the flapping motion), which in turn mitigates the drag penalties and negative lift experienced by the test ornithopter during this portion of its wing beat cycle.

While the results of Billingsely's experiment show an increase in net lift, the results also show that significant thrust penalties were incurred. It was concluded that more sophisticated wing kinematics are required in order to maintain the lift gains while mitigating thrust penalties, thus improving the overall aerodynamic performance of the ornithopter. The desired kinematics can be found in natural flyers. A bio-inspired gait known as the Continuous Vortex Gait (CVG) is shown in Figure 1 [13]. The front view in Figure 1 shows the wing bending, the side view shows that wing twist, and the top view shows the wing sweep at mid downstroke (left) and mid upstroke (right). A detailed discussion of the kinematics of CVG can be found in References 2 and 3. The advantage of using the CVG is that it can be implemented passively because it requires motion in only one major joint, namely the wrist.

In order to implement the CVG on a test ornithopter and to achieve improved performance, specific wing kinematics are required. The outer section of the wing has to bend, sweep and twist simultaneously during the upstroke, while remaining fully extended during the downstroke. The wrist, as shown in Figure 1, is the primary joint responsible for the radical shape changes in the CVG gait. In order to implement the CVG kinematics, a compliant mechanism called a compliant spine was placed in the location where an avian wrist would exist, namely at 37% of the wing half span [2]. Figure 2 shows a schematic of the compliant spine and its location along the leading edge spar of an ornithopter.
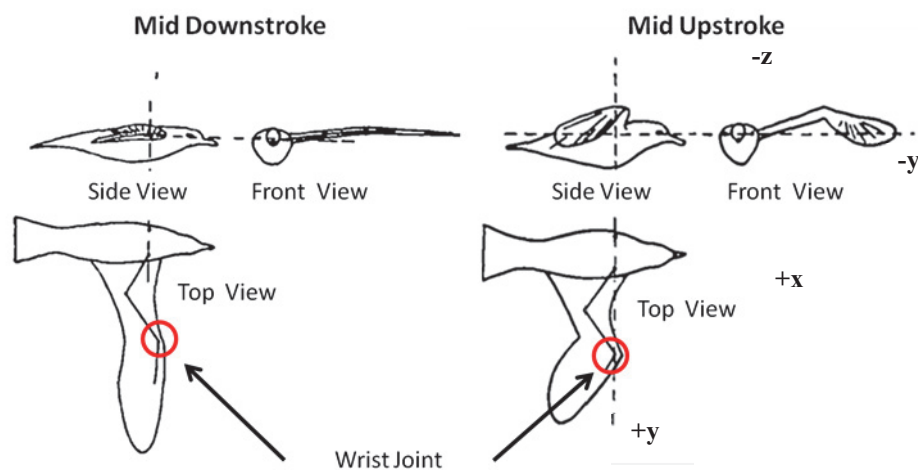
Figure 1. During the continuous vortex gait the wings are fully extended at mid downstroke (left) and out of plane bent, twisted and swept at mid upstroke (right) [13]
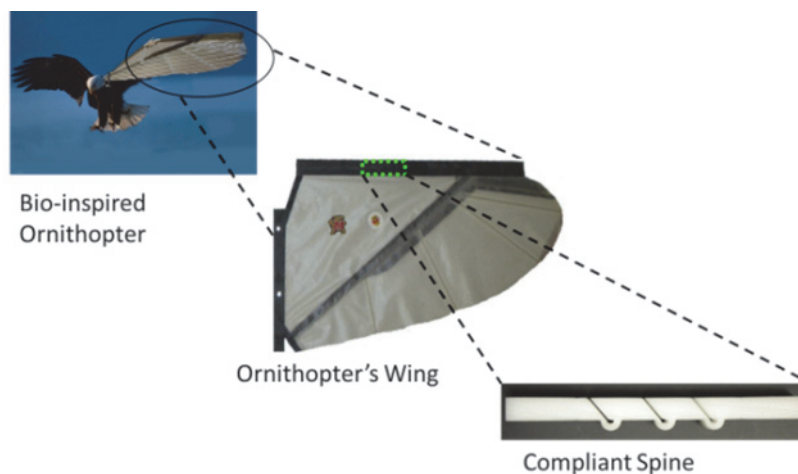
Figure 2. The compliant spine is inserted into the leading edge spar to mimic the function of an avian wrist.

2.2. Compliant Spine Design Optimization

In order to implement the CVG, a 3DOF motion is required, namely bending, sweep and twist. The focus of this paper, however, is using the compliant spine (CS), which is a 1DOF mechanism that allows for bending only, to achieve passive wing morphing. Other papers published by the authors focus on the design optimization and testing of bend-sweep and twist compliant mechanisms [14, 15]. The compliant spine is a novel, monolithic, nonlinear contact-aided compliant mechanism. Compliant mechanisms have numerous advantages over rigid-link mechanisms. They are easier to manufacture and have lower cost because they are usually monolithic in nature. During the upstroke, the compliant spine must allow the wing to morph in the bending direction, while during the downstroke, it must become stiff, mimicking a rigid spar. A schematic illustrating the desired stiffness of a compliant spine compared to the rigid spar and to a torsional spring is shown in Figure 3(a) [16]. In the figure, the Y-axis represents the integrated lift force produced by the wings over one flapping cycle and applied at the tip of the compliant spine as a conservative assumption. The X-axis represents the compliant spine tip bending deflection, $Z_{deflection}$. As illustrated, the desired stiffness of the compliant spine is nonlinear. It is stiff in the downstroke, similar to that of a rigid spar, and flexible in the upstroke, similar to a torsional spring. Figure 3(b) shows a CS design with three compliant joints. The design is flexible in bending during upstroke because of the compliance of the semi-circular compliant hinges, and it is stiff in bending during downstroke because the slanted faces come into contact with one another.

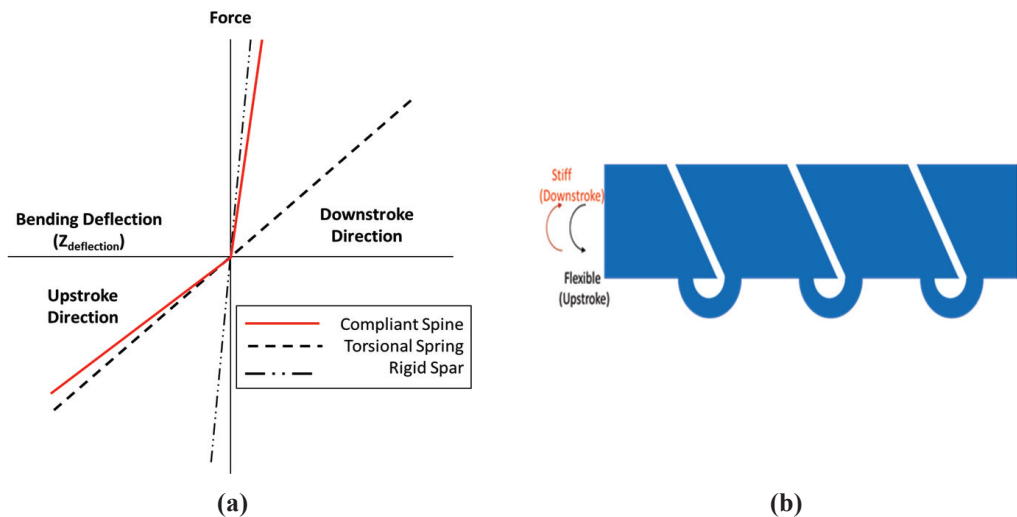<div align="center">(a)   (b)</div>

Figure 3. The desired stiffness of the compliant spine is nonlinear. The Y-axis represents the forces during a flapping cycle and the X-axis represents the compliant spine tip bending deflection (b) Schematic of a compliant spine with three compliant joints.

An optimization procedure was initially implemented to design a single compliant hinge with a single compliant joint [9, 16-18]. Later, an optimization procedure involving steady state dynamic analysis was performed on compliant spines with more than one compliant joint. This procedure yielded a family of designs that met the requirements for maximum von-Mises stress, and desired wing bending deflections. Figure 4 shows the typical von-Mises stress distribution in a three joint compliant spine at mid upstroke and mid downstroke. The number of compliant joints and the shape of each compliant joint affect the performance of the compliant spine. The design parameters that affect the joint's stiffness during the upstroke were related to the shape of the compliant hinge, while the design parameters that affect the downstroke stiffness were related to the geometry of the contact surfaces.
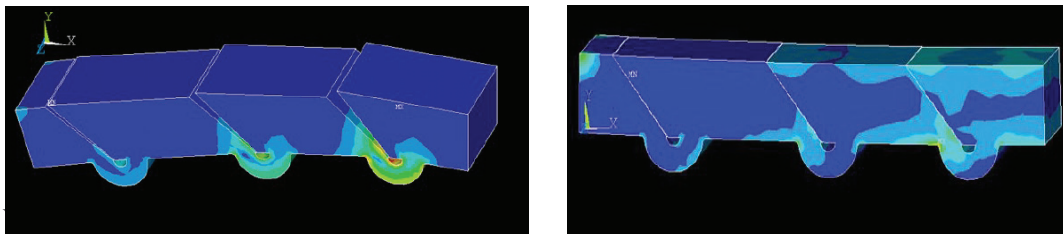

Figure 4. Typical von-Mises stress distribution of a three hinge compliant joint at mid upstroke (right) and mid downstroke (left).

Several compliant spines were tested during the flight test. Figure 5 shows all compliant spine designs tested. Each compliant spine design was given a name designation consisting of a number and two letters (e.g. 4PM). The number in the name of the compliant spine referred to the design number assigned by the optimization algorithm. The two letters in the name referred to the loading condition under which this compliant spine was designed. During the optimization procedure, the lift force distribution was approximated as a bending moment applied at the tip of the CS. The magnitude of the pure moment (PM) applied on the CS was assumed to be the maximum moment that the CS saw when a tip load, representing the integrated lift load [17, 18], was applied. Figure 6 shows the pure moment loading condition as well as the boundary conditions. In reality, the CS experiences a lift load distribution that is a combination of both moment and bending loads. The design optimization procedure implemented is described in detail in References 16 through 18.
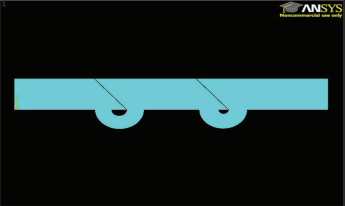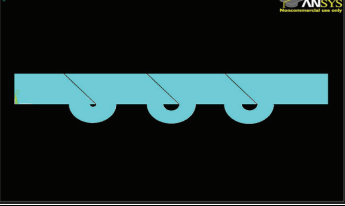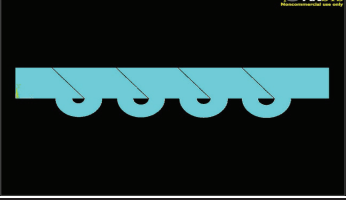
CS Design Name	CS Design Geometry
Comp 4PM	
Comp 14PM	
Comp 24PM	

Figure 5. The geometry of the three compliant spine designs tested during the free flight tests
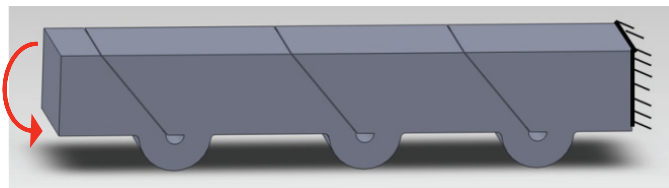

Figure 6. Compliant spines were assumed to have clamped-free boundary condition and were designed using pure moment (PM) loading condition

3. EXPERIMENTAL PROCEDURES

Several flight tests were conducted in order to assess the performance of the ornithopter equipped with various compliant spine designs. The flight tests were conducted at the Wright Patterson Air Force Base (WPAFB) in the Air Force Research Lab's (AFRL) Indoor Small Unmanned Aerial Systems (SUAS) laboratory. This facility is the largest Vicon® motion capture system lab in the United States. This section describes the ornithopter preparation, test configurations flown, equipment used, and the experimental set-up. Figure 7 shows a picture of the flight test chamber in the SUAS lab.
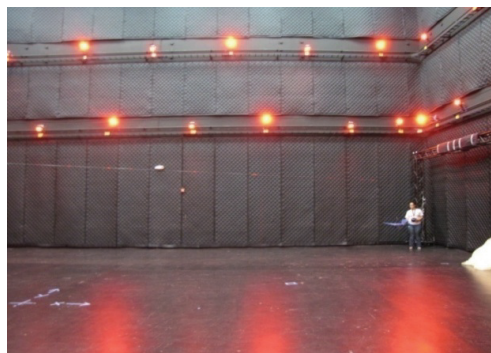

Figure 7. Test chamber in the Air Force Research Lab Small Unmanned Aerial Systems flight lab.

The AFRL SUAS indoor flight test laboratory is composed of an enclosed flight test chamber and a control room. The test chamber is a large, instrumented room where vehicles can be flown. It is roughly 16.8 m x 21.3 m x 10.6 m (55 ft. x 70 ft. x 35 ft.). SUAS lab instrumentation consists of a Vicon® motion capture system with 60 motion capture cameras. By adding small retro-reflective markers to a vehicle, the Vicon® system can track position and orientation of the vehicle with an accuracy of about 1.0 mm. The control room was used to process and record test data, such as vehicle position/orientation, velocity, acceleration, commands, sensor telemetry, and video-stream and audio data. More details about the AFRL SUAS flight test laboratory can be found in References 19.

3.1. Ornithopter Wing Configurations

Four ornithopter wing configurations were tested. The first configuration tested was an ornithopter with a uniform, carbon fiber wing spar. This configuration is referred to as the solid configuration for the remainder of this paper. The remaining configurations were equipped with compliant wing spars. A compliant wing spar was defined as a carbon fiber spar with a compliant spine inserted at 37% of the wing half-span to mimic the function of the avian wrist. Three compliant spine designs were tested, thus there were four configurations (1 solid and 3 compliant). Table 1 includes common test platform specifications [20].

Table 1. Ornithopter specifications common across all test configurations.

Span	Max. Chord	Flapping Rate	Speed
1.07m (42")	0.28 m (11")	4 – 6 Hz	2.5-8.5 m/s (8.2-27.9 ft./sec)

Figure 8 shows an image of a Morpheus Lab custom-built test ornithopter (ML 101) with a solid leading edge spar. This model served as the test baseline. The mass of the solid wing spar configuration ornithopter including batteries, motor, current sensor, markers, and data logger was measured to be 528 g (1.16 lb.).
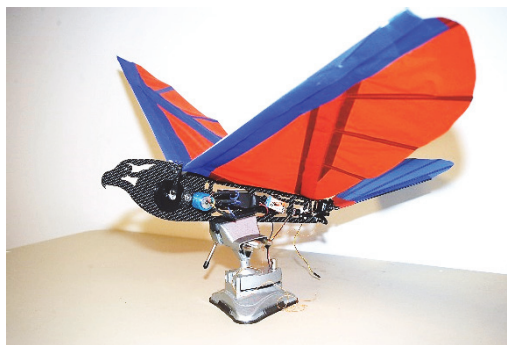

Figure 8. Test ornithopter with a rigid carbon fiber leading edge spar

3.1.2. Compliant Wing Spar Configurations

The same test ornithopter was flown for the compliant wing spar configurations. The only difference between the compliant and solid spar ornithopter wing configurations was the presence of a compliant spine design in the leading edge spar. All of the compliant spines were made from Delrin and were 63.5 mm (2.5") long with 25.4 mm (1") tabs on both sides to allow for attachment to the leading edge spar. The compliant spine was attached to the carbon fiber spar of the leading edge using six 5-40 bolts and a Delrin collar, as shown in Figure 9. The characteristic differences between the various compliant spine designs are the number of compliant hinges and the compliant joint geometry. Table 2 lists the compliant spine designs tested, the number of compliant hinges, and the total mass of the ornithopter with these spines inserted in its leading edge spar and including all the components that was previously present in the solid configuration.
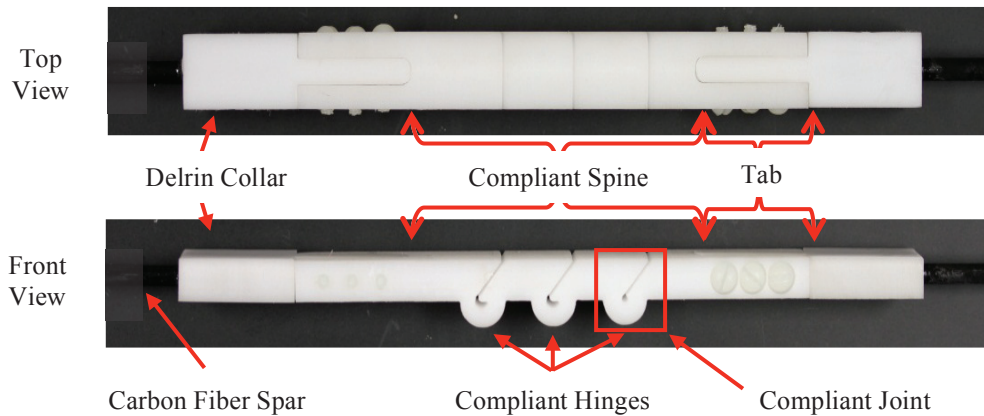
Figure 9. Compliant spine assembly components

Table 2. Specifications of compliant spine designs

Design Name	Number of Compliant Joints	Ornithopter Mass
Comp 4PM	2	611 g (1.35 lb.)
Comp 14PM	3	614 g (1.35 lb.)
Comp 24PM	4	612 g (1.35 lb.)

3.2. Test Platform Experimental Setup

Fifty-three reflective spherical markers were attached to the test vehicle in locations that were deemed necessary in order to obtain sufficient data to fully determine the vehicle wing and body kinematics. Out of the fifty-three markers, forty-four 6.35mm (0.25") diameter markers were placed in an asymmetrical pattern on the wings in order to aid in down range tracking. The other 9 markers were distributed as follows: 5 were placed on the fuselage to determine the ornithopter's body kinematics, 3 were placed on the tail to record user control inputs and 1 was placed at the wing root to measure the wing angle during a given flapping cycle. Figure 10 shows the placement of the wing reflective markers. Markers were distributed over both wings to balance the weight and they were placed asymmetrically to aid with tracking and post-processing. Data was collected at a sampling rate of 200Hz during these tests. The Vicon® motion capture system was used to capture and contrast the ornithopter wing 3D kinematics with and without the compliant spine inserted in the leading edge spar.

6.35 mm-diameter hemi-spherical reflective markers
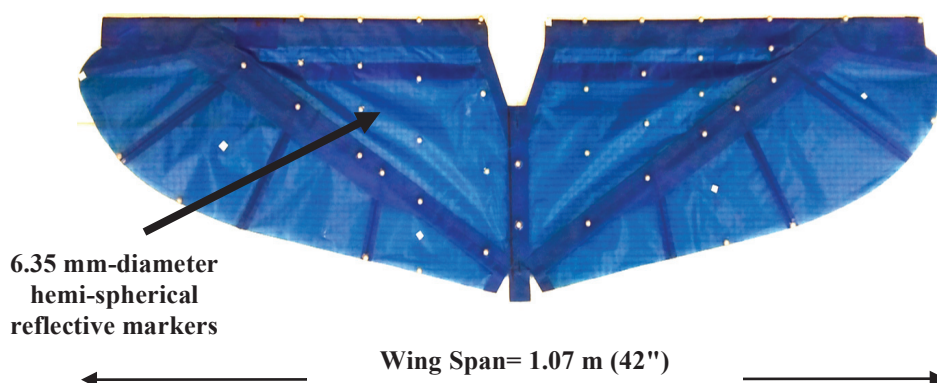
Wing Span= 1.07 m (42")

Figure 10. Wing reflective markers placement

In addition to the Vicon® markers, a current sensor was attached to the ornithopter body and was connected in series between the electric speed controller (ESC) and the battery in order to measure the current drawn by the motor. The data was recorded using an onboard Logomatic v2 Serial SD data logger. Figure 11(a) and Figure 11(b) show a schematic of the current sensor connection and a picture
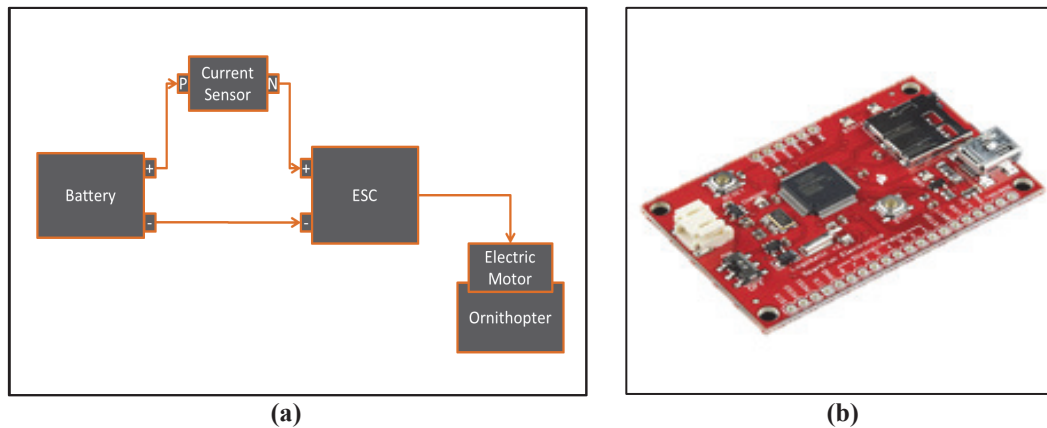
(a)　　　　　　　　　　　　　　　　(b)

Figure 11. a) Schematic for current sensor connection, showing the current sensor connected in series between the electric speed controller and the battery. b) Logomatic v2 Serial SD data logger used to record the current sensor output.

of the data logger, respectively. The voltage was supplied during the test using a 1350mAh, 3S, 11.1V, G6 Pro Lite 25C Lithium Polymer battery. The voltage supplied by the battery was recorded at the beginning of each flight and was assumed constant during a given test run. Each flight test run averaged between 10 to 15 seconds.

3.3. Flight Testing Technique

To aid in test data repeatability and prevent vehicle impacts with the chamber walls, a low-friction tether was utilized to guide the vehicle within the test chamber. The vehicle was suspended from a lead wire hung from this tether in order to restrain its flight path. Results shown in Section 4.1 confirms that above a certain height, the vehicle was no longer hanging on the lead line but is in free flight. The lead line was able to slide along the tether by using a barrel swivel attachment. The tether was strung horizontally between two trusses at opposite corners of the flight lab, at 2.1 m (7 ft.) height in order to maximize flight distance and keep the test vehicle at a height where camera coverage is ideal. The tether also prevented the vehicle from leaving the region where high-speed cameras were recording the flight. A wire crimp and a braking tether were used at the end of the flight path in order to arrest the vehicle at the end of each test run. Figure 12 shows a schematic of the test setup.
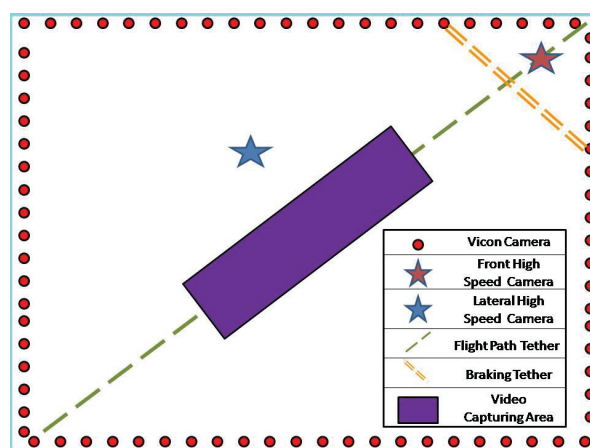

Figure 12. Test setup schematic showing the Vicon® cameras (representative), high-speed cameras, flight path, braking tether, and video capturing area

4. ORNITHOPTER KINEMATICS RESULTS

This section presents the free flight experiment results and is divided into three main sub-sections. The first sub-section explains the characteristics of a test ornithopter's free flight wing and body kinematics. The second sub-section discusses the effect of the presence of the compliant spine on the leading edge spar deflections. Lastly, the third sub-section introduces several flight metrics to compare the overall vehicle performance with and without the compliant spine inserted in the wings.

4.1. Ornithopter's Free Flight Kinematics

One of the goals of these flight tests was to extend the current database of steady level free flight data for avian-scale ornithopters. In order to attain this goal, consistent and repeatable kinematics over several flapping cycles were required. Before presenting the collected flight test data, the inertial reference frame, C_I and body fixed frames, C_0 used during this test are defined as shown in Figure 13.

The inertial reference frame is defined in accordance to the north, east, down (NED) convention and the body axis is defined where the axes are pointing out the nose, right wing, and underside of the ornithopter. Both reference frames are in accordance with standard aircraft body axes convention [21]. As such, a negative Z position indicates upwards displacement and a positive Z position indicates downwards displacement. Figure 13 also shows the naming convention for the position vectors. For example, $\mathbf{r}_{0,I}$ was defined as the position vector of the center of mass of the fuselage with respect to the inertial frame. Moreover, $\mathbf{r}_{p,I}$ and $\mathbf{r}_{p,0}$ were defined as the position vector of any point, p, on the vehicle with respect to the inertial reference frame and the body reference frame, respectively.
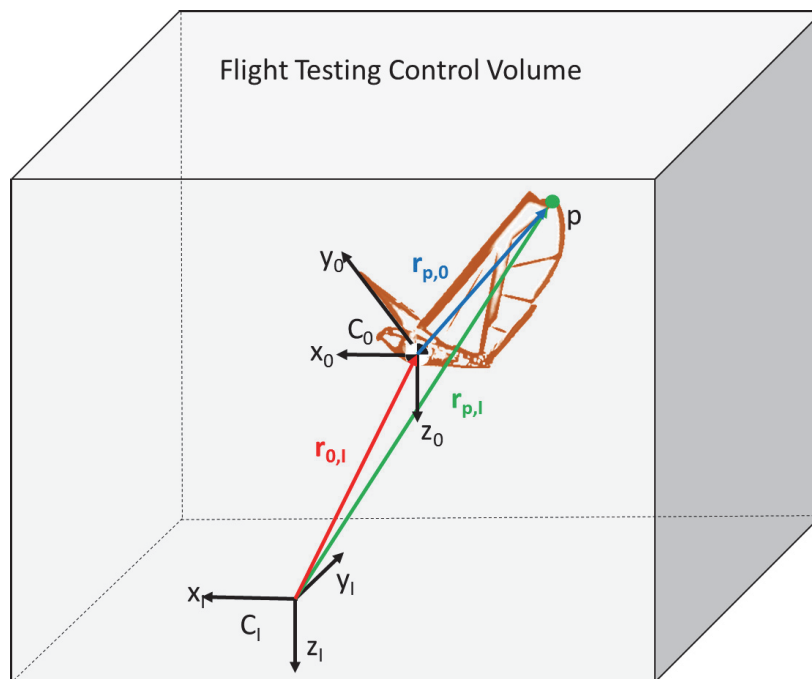

Figure 13. The flight testing control volume, showing the inertial, CI, and body fixed, C0, coordinate systems along with the position vector naming conventions.

Figure 14 shows the measured X, Y and Z positions of the 53 markers that were mounted on the ornithopter relative to the inertial reference frame, C_I. The figure also illustrates that repeatable tracking was achieved. The plot extends over eight consistent flapping cycles and represents a duration of 1.5 seconds of flight data. In order to estimate the accuracy of the markers' location and tracking, the ornithopter was placed in the middle of the control volume and the variances of the markers X, Y, and Z locations were computed. The maximum standard deviation was 0.10 mm, 0.10 mm, and 0.12 mm for the X, Y, and Z markers location, respectively. However, not only was it required that consistent and repeatable kinematics be achieved, but also this data needed to be recorded during steady level free flight. Figure 15 shows the side view of the 53 tracked markers during the eight consecutive flapping
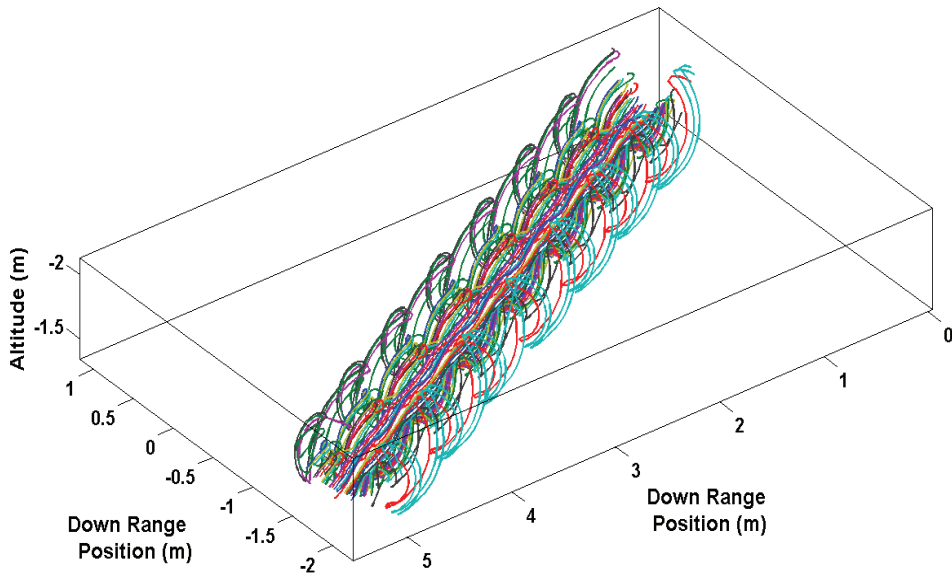
Figure 14. X, Y, and Z position of the 53 markers mounted on the ornithopter showing over eight flapping cycles of consistent and repeatable kinematics. The X and Y position represents the down range location of the marker and the Z position represent the marker's altitude with respect to the inertial frame of reference.

cycles shown in Figure 14. The plot confirms that the ornithopter is in steady level flight. Moreover, Figure 16 shows the Z position above ground level (AGL) of the center of mass of the ornithopter's fuselage with respect to the inertial frame, $r_{z\,0,I}$. The location and orientation of the fuselage's center of mass was calculated by fitting a rigid body to the fuselage using the five markers that were mounted on it. More details about this technique can be found in Reference 21. The black line in Figure 16 represents a threshold altitude above which the vehicle is no longer hanging on the tether and therefore is in free flight. Thus from the figure, it can be concluded that the ornithopter was flying well above this threshold altitude and therefore this flight test was successful in measuring and recording the ornithopter's kinematics over several flapping cycles and during steady level flight.
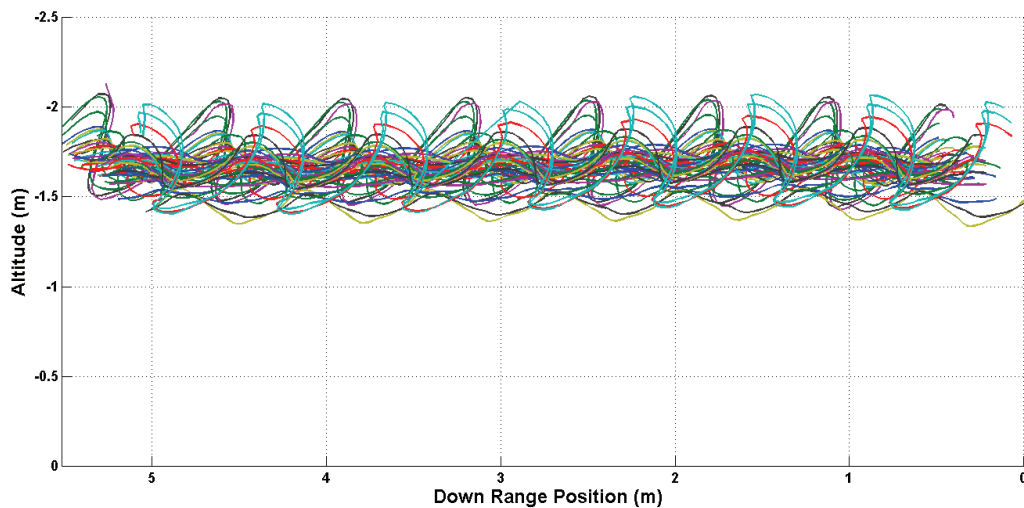

Figure 15. Side view of the 53 tracked markers showing over eight flapping cycles of steady level flight.
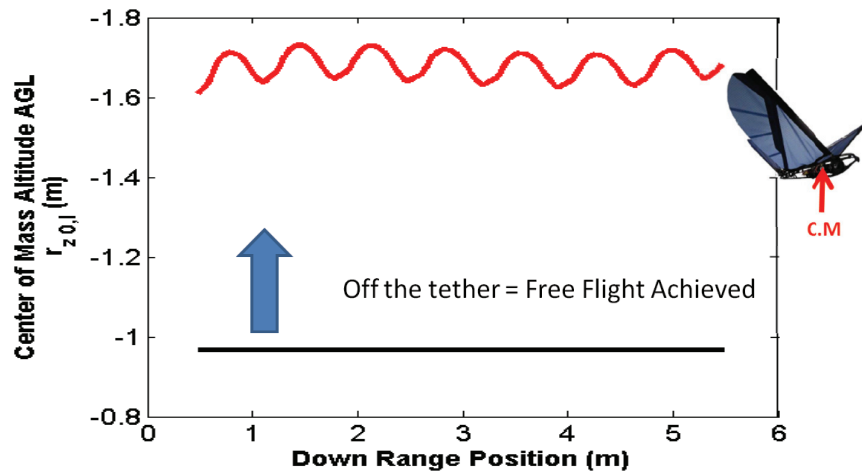
Figure 16. Ornithopter fuselage's center of mass altitude (red line) showing that the test ornithopter is flying above the altitude threshold (black line) for free flight.

After establishing free flight, the ornithopter kinematics was examined. Figure 17 compares the Z position above ground level in meters of the right wing tip marker ($r_{z\ wt,I}$) and the fuselage's center of mass ($r_{z\ 0,I}$) for 2.5 flapping cycles. The figure shows that the ornithopter's body position is out of phase with the wing tip position; in other words, as the wing flaps downwards, the fuselage is moving upwards and vice versa. Figure 17 also shows the ornithopter's body kinematics, an aspect of the vehicle's flight physics that is only possible to monitor through free flight testing.
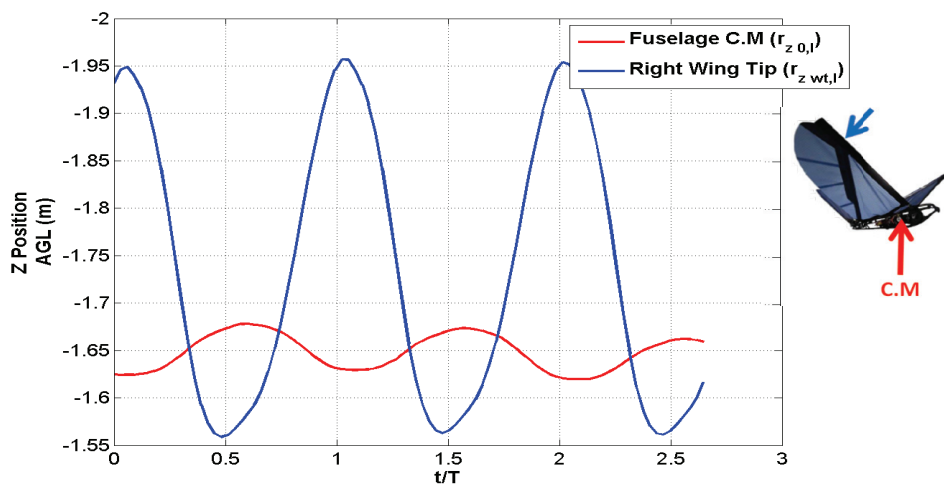

Figure 17. The altitude above ground level of the right wing tip marker (blue) and the fuselage's center of mass (red) versus time, normalized by the period of one flapping cycle.

In order to further understand the body kinematics, the Z position of the fuselage center of mass with respect to the inertial frame, $r_{z\ 0,I}$, was differentiated twice to obtain the center of mass vertical acceleration, $a_{z\ 0,I}$. Figure 18 shows the wing tip Z position with respect to the body frame in meters, $r_{z\ wt,0}$, and the fuselage center of mass acceleration with respect to the inertial frame in gs, $a_{z\ 0,I}$.
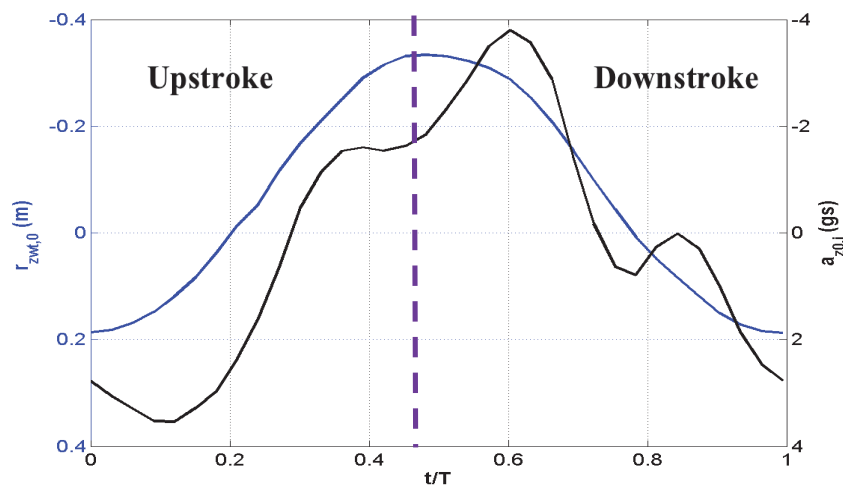
Figure 18. Wing tip marker Z-position with respect to the center of mass (blue) and the center of mass acceleration (black) versus time normalized by the period of one flapping cycle

The significance of the body dynamics is apparent in Figure 18. The body of the baseline or non-compliant ornithopter has an acceleration of ± 4 gs. During prior [22] and current flight tests, it was noticed that the vertical acceleration had a peak after the upstroke-downstroke transition and downstroke-upstroke transition points. Prior to these flight tests, the reason for this peak remained unexplained, these free flight tests attributes these peaks to the thrust flap portion of the wing. The thrust flap is shown in Figure 19 and it is the part of the wing primarily responsible for the thrust production. The thrust flap lags the main wing leading edge spar in changing directions at both stroke transition points. Figure 20 shows the Z position of the wing tip and the thrust flap with respect to the body frame, along with the vertical acceleration of the center of mass with respect to the inertial frame. The figure shows that the peaks that occur after the transition points, marked by the red circles, are due to the thrust flap portion of the wing changing directions. In other words, the thrust flap can be thought of as a hinged flat plate that when changes direction, it causes an increase in the body's acceleration. Figure 19 also shows the location of the wing tip and thrust flap markers.

Figure 19. Wing planform showing the thrust flap region and the locations of the wing tip and thrust flap markers.
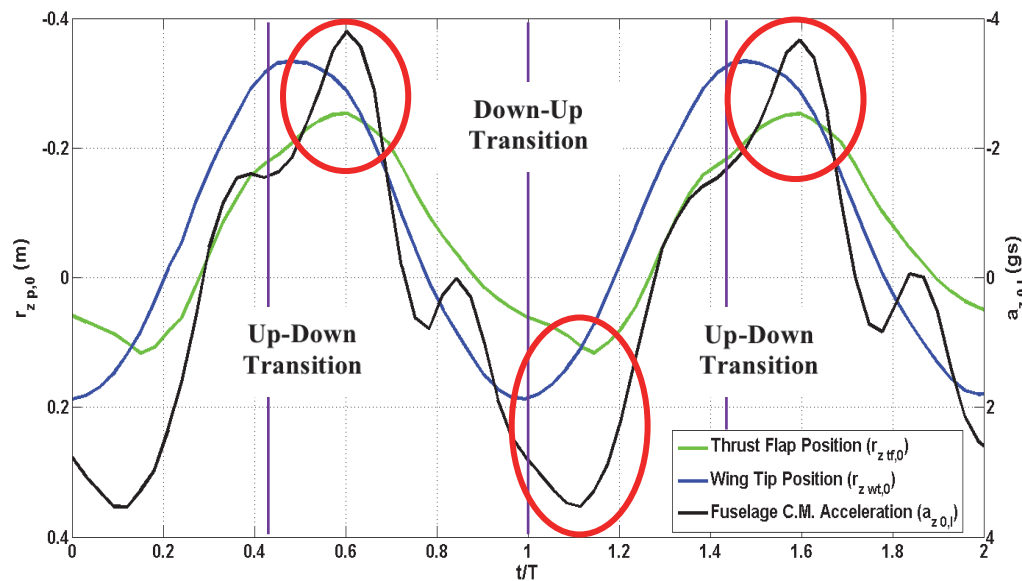
Figure 20. Wing tip marker Z-position with respect to the center of mass (blue), thrust flap marker Z-position with respect to the center of mass (green), and the center of mass acceleration (black) versus time, normalized by the period of one flapping cycle. The figure shows the positons and acceleration for two flapping cycles.

4.2. Effect of Compliant Spine Presence on Leading Edge Spar Deflection

For the flight tests, the three compliant spine designs described in 2.2 were inserted into the wing leading edge spar. This section details the effect of the presence of the compliant spine on the leading edge spar bending deflection. During the upstroke, the compliant spine experienced passive bending due to the presence of the compliant joints. Figure 21 shows the Z deflection of the markers placed at the leading edge spar during the upstroke for both the solid and Comp 24PM wing configurations. The Z deflection for the leading edge spar markers was referenced to the body frame.

The compliant spine design optimization predicted that a compliant spine with a larger number of compliant hinges tends to have a greater maximum bending deflection. Only results from designs Comp 24PM and Comp 4PM are shown in this section because these designs had the most and least number of compliant hinges, respectively. Figure 22 show the Z deflection of the markers placed on the right wing leading edge spar, at mid upstroke and mid downstroke. The figure confirms the design optimization predication that Comp 24PM is more flexible than design 4PM and therefore has a larger bending deflection.

At mid upstroke, the relative bending deflection between the compliant spar tip marker and the solid spar tip marker was 110.7 mm (4.35") and 83.24 mm (3.28") for the Comp 24PM and Comp 4PM designs, respectively. During the downstroke, upwards bending is observed, this bending occurs during the downstroke due to the presence of the contact gaps and flexibility of the Delrin[TM] material itself. The relative bending deflection between the compliant spar tip marker and the solid spar tip marker was 94.3 mm (3.71") and 72.6 mm (2.86") for the Comp 24PM and Comp 4PM designs, respectively. Overall, the downwards bending deflection of the compliant spines during the upstroke was greater than the upwards bending deflection during the downstroke by 17 % for Comp 24PM and 14% for Comp14 PM, thus an asymmetry in the wings kinematics was achieved due to the presence of the compliant spine.
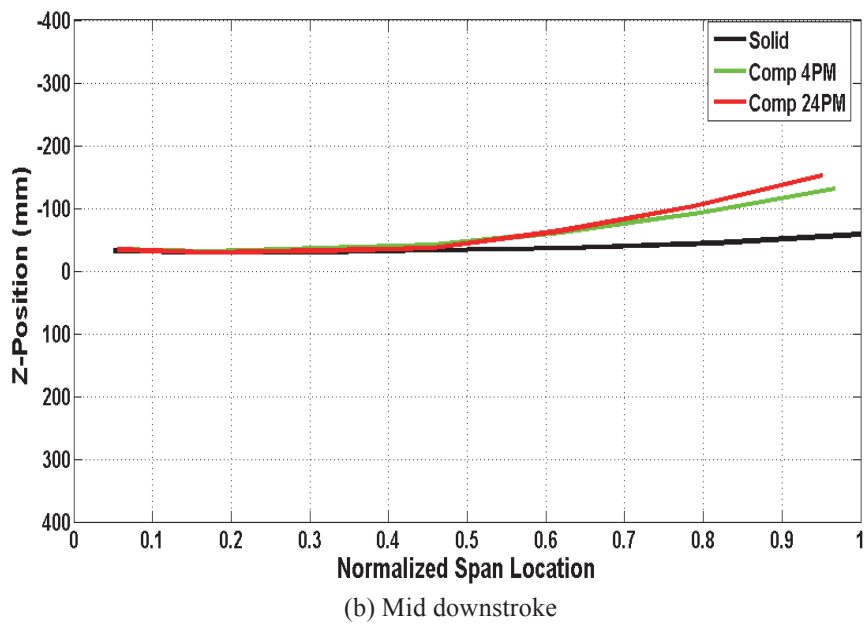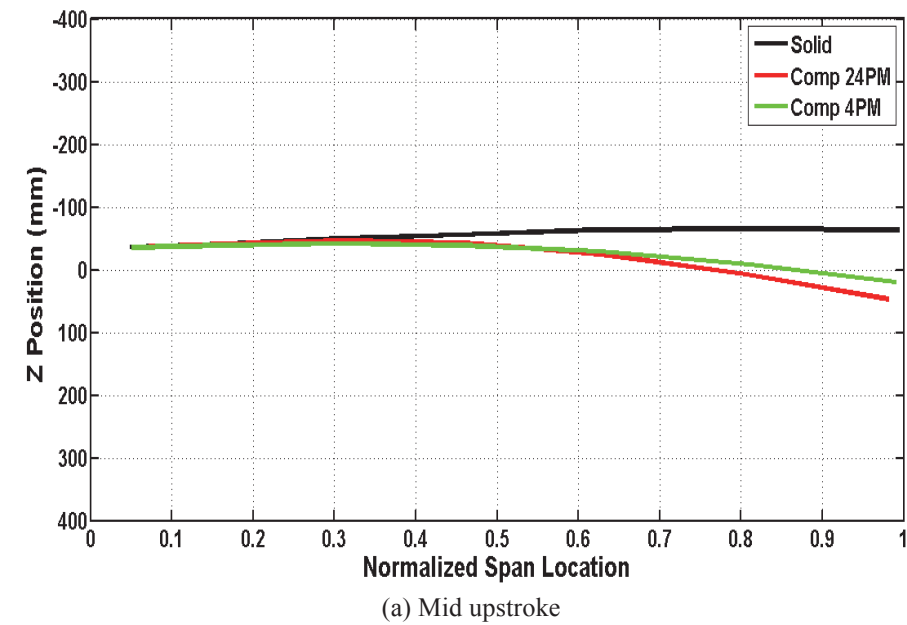
(a) Mid upstroke

(b) Mid downstroke

Figure 22. The Z position of the reflective markers mounted at the right wing leading edge spar versus the normalized span location at mid upstroke (top) and mid downstroke (bottom).

4.3. Effect of Compliant Spine Presence on Overall Vehicle Performance

This section discusses the effect of the presence of the compliant spine on the vehicle's performance. Several metrics were used to evaluate the vehicle's performance. These metrics can be divided into three categories: power expenditure, horizontal propulsive force and vertical propulsive force.

4.3.1. Power Expenditure

Most morphing wing mechanisms presented in the literature show performance benefits, however they suffer from weight penalties that necessitate additional power expenditures that mitigate the

performance gains [7, 23]. The first metric that was used to evaluate the performance of the compliant and non-compliant ornithopter wing was the specific power. Specific power was defined as the electric power withdrawn by the flapping wing drive motor normalized by the mass of the ornithopter platform. Figure 23 shows a plot of the mean specific power over one flapping cycle for the compliant and solid leading edge wing spar configurations. The figure shows that when normalized by the mass of the various configurations, the power expenditure of the compliant versus non-compliant configurations is comparable. Consequently, carrying the additional weight of the compliant spines, as compared to the lower weight of the rigid spar, does not cost the vehicle any significant penalty from a power consumption stand point. The most compliant and heaviest configuration, namely Comp 24PM, has less than 5% penalty in specific power when compared to the solid configuration.
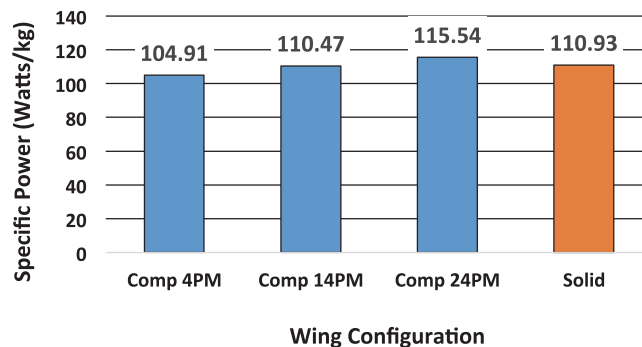

Figure 23. Mean specific power over one flapping cycle for the compliant and solid, non-compliant, wing configurations.

4.3.2. Horizontal Propulsive Force

The second group of metrics used to compare the performance of the test ornithopter with and without the presence of the compliant spine was related to the horizontal acceleration of the center of mass with respect to the inertial frame, $a_{x\,0,I}$. The horizontal acceleration can be related to the vehicle's thrust production. According to the body fixed frame of reference, a positive $a_{x\,0,I}$ corresponds to forward flight. Rather than using $a_{x\,0,I}$ directly to compare the effect of the various compliant spines, an additional metric that is common in the literature, namely the horizontal load coefficient, C_X is used [24].The expression for C_X is shown in Equation 1 and it is the coefficient of propulsive force in the horizontal direction.

$$C_x = \frac{m\overline{a_{x\,0,I}}}{\frac{1}{2}\rho V_f^2 S} \tag{1}$$

where, m is the vehicle's mass, ρ is the air density, V_f is the mean forward velocity, S is the wing area and $\overline{a_{x\,0,1}}$ is the mean horizontal acceleration of the center of mass over one flapping cycle. C_X is the non-dimensional form of the mean horizontal force generated by the ornithopter over one flapping cycle. A more intuitive way to explain C_X is that, for a given distance per unit time, a vehicle that has a larger value of C_X will have more propulsive power in the horizontal direction.

Figure 24 compares the values of C_X for the solid, Comp 4PM, Comp 14PM, and Comp 24PM wing configurations. The figure shows that Comp14PM, Comp 24PM, and Comp 4PM improve the coefficient of horizontal propulsive force. When comparing the values of C_X for the compliant and non-compliant wing spar configurations, it should be noted that Comp 14PM has the highest propulsive force in the horizontal direction.
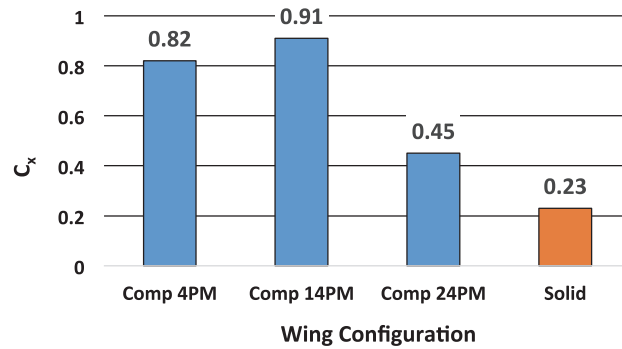
Figure 24. Coefficient of mean horizontal propulsive force for the compliant and solid, non-compliant, wing configurations.

The second metric related to the horizontal propulsive force is called the power loading and it is defined as C_X/C_P [24]. The horizontal power loading metric describes the amount of horizontal force that can be generated per unit power consumed, thus maximizing this quantity would indicate that the vehicle is able to generate a given amount of horizontal force efficiently. C_P is defined in Equation 2 and it is the non-dimensional mean electric power consumed over one flapping cycle [24].

$$C_p = \frac{\bar{P}}{\frac{1}{2}\rho v_f^3 S} \tag{2}$$

where, $\bar{P}$ is the mean power consumed over one flapping cycle. The values of the horizontal power loading for the compliant and non-compliant configurations shown in Table 3 indicates that the ornithopter with Comp14PM wing spar configuration can generate horizontal propulsive force more efficiently than any of other configurations tested. Thus, Comp 14PM offers the best design for horizontal propulsive force production and therefore thrust and range. This is explained through further analysis of the effect of compliance on the mean horizontal acceleration of the center of mass during the upstroke and downstroke, separately. Data from this flight test shows that the compliance achieved during the upstroke causes penalties to the mean horizontal acceleration produced, while compliance during the downstroke results in gains. Thus, Comp14PM offers the best compromise between up and down strokes compliance for horizontal force production.

Table 3. Values for horizontal power loading for the non-compliant and compliant wing spar configurations.

Wing Configuration	C_X/C_P
Solid	0.05
Comp 4PM	0.04
Comp 14PM	0.07
Comp 24PM	0.03

The third and final group of metrics used are related to the vertical acceleration of the center of mass with respect to the inertial frame, $a_{z\,0,I}$. According to the inertial frame of reference, negative vertical acceleration corresponds to upwards acceleration. Therefore a higher negative acceleration indicates an increase in the body's upwards acceleration and the wings' downwards acceleration, or an increase in the positive vertical propulsive force produced by the wings. Figure 25 shows the vertical acceleration of the body center of mass for the Solid, Comp 4PM, and Comp 24PM configurations versus time normalized by the period of one flapping cycle. Only the most and least compliant configurations are shown below for graphical clarity; Comp 14PM exhibits the same body center of mass vertical acceleration characteristics.
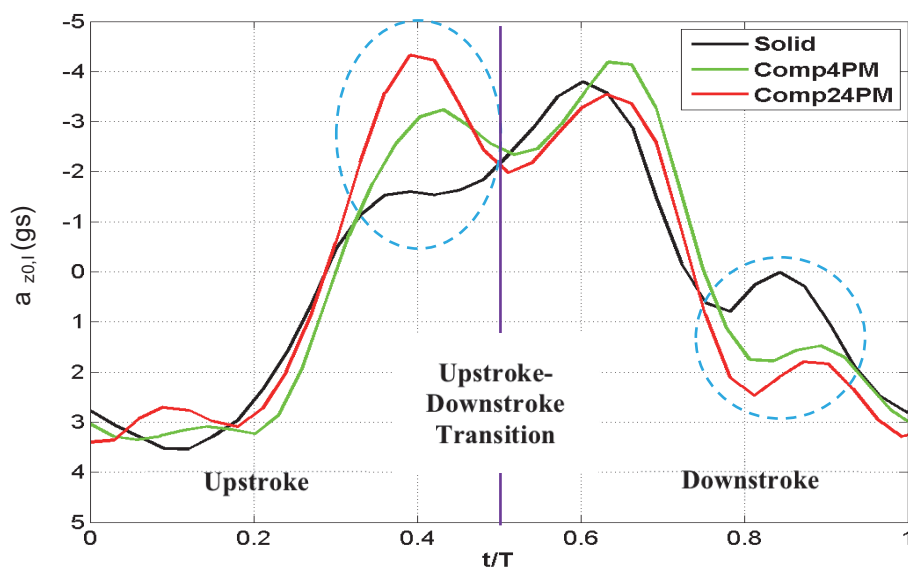
Figure 25. Vertical acceleration of the fuselage center of mass for the solid (black), Comp 4PM (green, and Comp 24PM (red) configurations versus time normalized by the period of one flapping cycle

The effect of the presence of a compliant spine in the leading edge spar is evident at two locations in the flapping cycle (marked by the dashed circles), as shown in Figure 25. The first location is at the end of the upstroke just before the upstroke to downstroke transition. At this point, the compliant spine is changing from the bent configuration to the locked configuration, creating an effect similar to a whip lash and increasing the body upwards acceleration. This increase in the body upwards acceleration increases the wings' downwards acceleration, which is a favorable effect. During the downstroke portion of the flapping cycle, the behavior of the ornithopter with and without the compliant spine was predicted to be similar because the contact surfaces in each compliant hinge come together. However, as mentioned in Section 4.2 , due to the presence of the contact gaps and the difference in Young's modulus between the material of the solid spar (uni-directional carbon fiber composite) and the material of the compliant spine itself (DelrinTM) some upwards bending occurs during the downstroke. The second location where the effect of the compliant spine is apparent is during the second half of the downstroke. At this point the compliant spine has locked completely and the upward bending has started to occur. Thus, during the second half of the downstroke, an increase in the body's positive acceleration is observed due to the presence of the compliant spine. A higher positive vertical center of mass acceleration indicates an increase in the body's downwards acceleration and wings' upwards acceleration and therefore an increase in the amount of negative vertical propulsive force produced by the wings, which is an adverse effect.

   A metric that is more common in literature, namely the vertical force coefficient, C_Z is also used to compare the effect of compliance on the vertical propulsive force generated by the ornithopter [24]. The expression for C_Z is shown in Equation 3 and it is the coefficient of propulsive force in the vertical direction.

$$C_Z = \frac{m\overline{a_{z\,0,I}}}{\frac{1}{2}\rho V_f^2 S}$$ (3)

Similar to C_X, C_Z is an indication of the propulsive force a vehicle can generate but in the vertical direction so, for a given distance per unit time, C_Z can indicate the amount of propulsive power a vehicle can generate. As such, the objective here is to minimize C_Z because, as explained before, a higher positive value for $\overline{a_{z\,0,I}}$ corresponds to more wings' upwards acceleration and more negative vertical propulsive force production. Table 4 shows the values of coefficient of vertical propulsive force, C_Z, for the solid, Comp 4PM, Comp 14PM, and Comp 24PM wing configurations. Thus, when comparing the values of C_Z for the compliant and non-compliant configurations shown in Table 4,

Table 4. Values for the coefficient of vertical propulsive force for the solid and compliant wing spar configurations.

Wing Configuration	C_Z
Solid	0.48
Comp 4PM	0.71
Comp 14PM	0.98
Comp 24PM	0.31

Comp 24PM has the lowest value of and thus the best performance from a vertical load production stand point. Moreover, because the objective is to minimize rather than maximize C_Z, it is not appropriate to use the power loading metric as previously used for the horizontal load coefficient.

5. CONCLUSIONS AND FUTURE WORK
The test results presented herein proved to be successful in producing consistent and repeatable flight data over more than eight free flight flapping cycles and several compliant spine configurations. Through these flight tests, the ornithopter body dynamics were shown to be significant, ±4gs for the solid configuration and with significantly different acceleration profiles with the compliant spines. The peak in the body's vertical acceleration that occurred after the upstroke-downstroke and downstroke-upstroke transition points was attributed to the kinematics of the thrust flap. The effect of the presence of the compliant spines in the wings on leading edge spar deflection was examined through the flight tests. Inserting the compliant spine into the leading edge spar introduced an asymmetry between the upstroke and the downstroke, as desired. However, the data shows that upwards bending occurs during the downstroke due to the flexibility of Delrin and the contact gaps. Several metrics were presented and used to compare the performance of the compliant and non-compliant or baseline ornithopter. The first metric used was the specific power; data showed that, when normalized by the vehicle's mass, the test ornithopter with any given wing configuration consumed a similar amount of electric power. The second group of metrics used were related to the horizontal force produced over one flapping cycle, results showed that Comp 14PM design improved the mean horizontal propulsive force the most when compared to the other wing-spar configurations. The third and last group of performance metrics were related to the vertical propulsive force produced over one flapping cycle. Comp 24PM design reduced the body's center of mass positive acceleration, which translates into overall vertical propulsive force gains. These flight tests showed that passively morphing the wings through introducing compliance in the leading edge spar is not only possible and requires no additional power expenditure but it is also beneficial to the overall vertical and horizontal propulsive force production.

Future work includes performing an analytical stability analysis of the leading edge spar, to determine any compliant spine stiffnesses for which the system becomes unstable. This model will be used as a design tool that will guide future design optimization of multi-degree of freedom compliant elements. In addition, a quantitative comparison between the free flight tests results and constrained flight test results will be conducted. This is important because, if both tests results are similar, then being able to predict free flight performance of the ornithopter from constrained flight testing would be more cost efficient and much more feasible. Finally, it is recommended that in future flight tests, vehicle accelerations and orientations are measured directly using onboard inertial measurement units that include accelerometers and gyroscopes.

REFERENCES

[1] Shyy, W. Berg, M., and Ljungqvist, D."Flapping and flexible wings for biological and micro air vehicles", *Progress in Aerospace Sciences*, (1999) 35: 455-505

[2] Tobalske, B.W., and Dial, K.P. "Flight kinematics of Black-billed Magpies and pigeons over a wide range of speeds", *Journal of Experimental Biology*, (1996) 99: 263-280.

[3] Tobalske, B.W. "Physiology and Biomechanics of Gait Selection in Flying Birds", *Physiol Biochem Zool.*, (2000) 73(6):736-50.

[4] Fenelon, M.A.A., and Furukawa, T. "Design of an Active Flapping Wing Mechanism and a Micro Aerial Vehicle Using a Rotary Actuator." *Mechanism and Machine Theory* 45 (2009): 137-46.

[5] McDonald, M., and Sunil K. Agrawal. "Design of a Bio-Inspired Spherical Four-Bar Mechanism for Flapping-Wing Micro Air-Vehicle Applications." *Journal of Mechanisms and Robotics*, (2010) 021012

[6] Cox, A., Monopoli, D., Goldfarb, M., and Garcia, E. "Development of piezoelectrically actuated micro-aerial vehicles", *SPIE Symposium on Microrobotics and Microassembly*, vol. 3834, pp. 101-108, September 1999.

[7] Conn, A., Burgess S., and Ling C., "Design of a parallel crank-rocker flapping mechanism for insect-inspired micro air vehicles," *Journal of Mechanical Engineering Science*, vol. 221, pp. 1211-1222, 2007.

[8] Cox A., Monopoli, D., Cveticanin, D., Goldfarb, M., and Garcia, E., "The Development of Elastodynamic Components for Piezoelectrically Actuated Flapping Micro-air Vehicles," *Journal of Intelligent Material Systems and Structures*, vol. 13, pp. 611-615,September 2002.

[9] Wissa, A., Tummala, Y., Hubbard Jr., J. E., and Frecker, M. "Passively Morphing Ornithopter Wings using a Novel Compliant Spine: Design and Testing," *Smart Materials and Structures* (2012) 21094028

[10] Wissa, A., Tummala Y., Hubbard Jr., J. E., Frecker M., and Brown, A. "Testing of novel compliant spines for passive wing morphing,"Proc. *Smart Materials, Adaptive Structures and Intelligent Systems Conf.* 2011-5198, Scottsdale, AZ

[11] Mueller D., Gerdes J., and Gupta, S.K. "Incorporation of passive wing folding in flapping wing miniature air vehicles." *ASME Mechanism and Robotics Conference*, August 30-September 2, 2009, San Diego

[12] Billingsley, D., Slipher, G., and Grauer, J., "Testing of a Passively Morphing Ornithopter Wing," *AIAA Paper* 2009-1828.

[13] Brown, R. H. "The Flight of Birds: Wing Function in Relation to Flight Speed." *Diss. University of Cambridge*, 1952.

[14] Tummala, Y., Frecker, M. I., Wissa, A. A. and Hubbard Jr, J. E., 2013, "Design and optimization of a bend-and-sweep compliant mechanism," *Smart Materials and Structures*, 22(9).

[15] Tummala, Y., Frecker, M., Wissa, A., Hubbard Jr., J. E., 2013, "Design Optimization of Twist Compliant Mechanism ", Proceedings of Smart Materials, *Adaptive Structures and Intelligent Systems Conference*, Snowbird, UT.

[16] Tummala, Y., Wissa A., Frecker, M., and Hubbard Jr., J. E. "Design of a passively morphing ornithopter wing using a novel compliant spine" Proc. Smart Materials, *Adaptive Structures and Intelligent Systems Conf.* 2010-3637, Philadelphia PA

[17] Tummala, Y. "Design and Optimization of Contact-Aided Compliant Mechanisms with Nonlinear Stiffness". Dissertation. University Park /Pennsylvania State University, 2013.

[18] Tummala, Y., Wissa, A., Frecker, M., Hubbard Jr., J. E., "Design Optimization of a Compliant Spine for Dynamic Applications", Proceedings of Smart Materials, *Adaptive Structures and Intelligent Systems Conference*, 2011, Scottsdale, AZ, United States.

[19] Kim J, Chan P, Jun A, Chung D, K J, Hwnag H, et al., "Flight Test Measurement and Assessment of a Flapping Micro Air Vehicle", *Journal of Aeronautical and Space Sciences*, (2012) 12, 238-249

[20] Harmon, R. "Aerodynamic Modeling of Flapping Membrane Wing Using Motion Tracking Experiments, Aerospace Engineering." Thesis. College Park / University of Maryland, 2009.

[21] Etkin, Bernard. *Dynamics of Flight: Stability and Control*. New York: Wiley, 1982. Print.

[22] Grauer J, Ulrich E, Hubbard J, Pines D, Humbert J S. "Testing and system identification of an ornithopter in longitudinal flight. " *Journal of Aircraft*, (2011) 48, 660–667.

[23] Barbarino, S., O. Bilgen, R. M. Ajaj, M. I. Friswell, and D. J. Inman. "A Review of Morphing Aircraft." *Journal of Intelligent Material Systems and Structures*, (2011) 22.9: 823-77.

[24] Zheng, L., T. Hedrick, and R. Mittal. "A Comparative Study of the Hovering Efficiency of Flapping and Revolving Wings." *Bioinspiration & Biomimetics* 8.3 (2013)